



Effects of sulfur doping on graphene-based nanosheets for use as anode materials in lithium-ion batteries

Young Soo Yun ^{a,c}, Viet-Duc Le ^b, Haegyeom Kim ^c, Sung-Jin Chang ^{d,h}, Seung Jae Baek ^e, Sungjin Park ^f, Byung Hoon Kim ^g, Yong-Hyun Kim ^b, Kisuk Kang ^c, Hyoung-Joon Jin ^{a,*}

^a Department of Polymer Science and Engineering, Inha University, Incheon 402-751, South Korea

^b Graduate School of Nanoscience and Technology, KAIST, and Center for Nanomaterials and Chemical Reactions, Institute for Basic Science (IBS), Daejeon 305-701, South Korea

^c Department of Materials Science and Engineering, Seoul National University, Seoul 151-742, South Korea

^d Division of Materials Science, Korea Basic Science Institute (KBSI), Daejeon 305-333, South Korea

^e Department of Nano Science and Technology, Seoul National University, Seoul 151-747, South Korea

^f Department of Chemistry and Chemical Engineering, Inha University, Incheon 402-751, South Korea

^g Department of Physics, Incheon National University, Incheon 406-772, South Korea

^h Department of Chemistry, Chung-Ang University, Seoul 156-756, South Korea



HIGHLIGHTS

- Sulfur-doped graphenes are utilized for anode materials in lithium-ion battery.
- Sulfur doping on graphenes contributes to the high specific capacity of the battery.
- A first-principles calculation shows good agreement with the experimental results.
- High rate performance is achieved by the improved electrical conductivity of anodes.
- A stable cycle life over 500 cycles is achieved at a high current density of 1488 mA g⁻¹ (4 C).

ARTICLE INFO

Article history:

Received 2 January 2014

Received in revised form

17 March 2014

Accepted 19 March 2014

Available online 27 March 2014

Keywords:

Lithium-ion battery

Anode

Graphene

Sulfur

Doping

ABSTRACT

Graphene-based nanosheets (GNS) have been studied for use in electrochemical energy storage devices. A deeper understanding about the system is required for achieving enhanced power output and high energy storage. The effects of sulfur doping on the electrochemical properties of GNS are studied for their use as an anode material in lithium-ion batteries. Sulfur doping in GNS contributes to the high specific capacity by providing more lithium storage sites due to Faradaic reactions. In addition, superior rate performance of sulfur-doped GNS (S-GNS) is achieved through the improved electrical conductivity of S-GNS (1743 S m⁻¹), which is two orders of magnitude higher than that of GNS (32 S m⁻¹). In addition, good cyclic stability of S-GNS is maintained even after 500 cycles at a high current density of 1488 mA g⁻¹ (4 C).

© 2014 Elsevier B.V. All rights reserved.

1. Introduction

Lithium-ion batteries (LIBs) have attracted considerable academic and industrial interest as an energy storage device owing to their ever-increasing and urgent demand in widespread applications such as portable electronics and electrical/hybrid vehicles [1].

As such, studies worldwide are focusing on developing LIBs with high reversible capacity, excellent rate capability, and good cycling stability [1–4]. But traditional graphite-based anode materials show low Li-storage capacity (372 mA h g⁻¹) owing to the limited Li ion storage sites (LiC₆) within the sp² carbon hexahedrons, and relatively low rate capability, owing to the intrinsic nature of the intercalation process [5,6].

Graphene, a single layer of sp²-hybridized carbon atoms, has attracted considerable interest for use in various applications because of its outstanding physical properties [7–9]. Single-layer

* Corresponding author. Tel.: +82 32 860 7483; fax: +82 32 865 5178.

E-mail address: hjin@inha.ac.kr (H.-J. Jin).

graphene with a disordered structure was speculated to form Li_2C_6 because both graphene surfaces can host Li ions [10–14]. In addition, heteroatoms, nanoscale cavities, and active defects such as edges and vacancies in graphene nanosheets have been suggested to accommodate additional Li ions [13,14]. Graphene-based nanosheets (GNS) induced by oxidation and reduction contain numerous oxygen heteroatoms, nanoscale holes, and defects owing to the imperfect restoration of the original sp^2 bonding character as well as the disordered structure [15,16]. Consequently, GNS can exhibit high Li ion storage capability. Furthermore, shortening the diffusion length of Li adatoms and increasing the electronic conductivity by doping in GNS can lead to fast kinetics [11,17,18]. Several studies have already achieved high electrochemical performances using defect-engineered GNS [19–22]. In particular, Wang et al. [19] reported that a GNS anode showed a reversible capacity of 650 mA h g^{-1} during the first charging cycle at a current density of 1 C within the voltage range 0.02–3.0 V and a specific capacity of 460 mA h g^{-1} even after 100 cycles. Guo et al. [18] reported a similar result. These properties of a GNS are closely related to oxygen content, which greatly enhances the electrochemical performance of the GNS anode.

Sulfur, a chalcogen, can be incorporated into carbon-based anode materials. Sulfur-doped carbon-based materials have been reported to show increased reversible capacity [23,24]. Moreover, sulfur-doped porous carbon hybridized with graphene has been reported to show high capacity and excellent rate performance [25]. These results suggest that sulfur doping can be used for enhancing the electrochemical performances of carbon-based anodes. But studies have not yet clarified the effects of sulfur doping as well as the effects of sulfur heteroatoms on LIB anodes. In addition, the use of sulfur-doped GNS (S-GNS) as an anode material for LIBs has not yet been attempted.

In this study, the effects of sulfur doping on GNS for potential use as an anode material for LIB were investigated. This study attempts the first fundamental understanding of the effect of sulfur in GNSs with the intention of gaining insights into GNS-based anode materials.

2. Experimental

2.1. Preparation of S-GNS and GNS

Graphene oxide (G-O) was prepared from natural graphite (Sigma–Aldrich) using the Hummers method. Aqueous G-O suspensions were frozen in liquid nitrogen and then freeze-dried using a lyophilizer (LP3, Jouan, France) at 50 °C and 4.5 Pa for 72 h. After lyophilization, low-density and loosely packed G-O powders were obtained [26]. 100 mg of the as-obtained lyophilized G-O powder and 100 mg of elemental sulfur powder (Sigma–Aldrich, 99.98%) were mixed in a mortar. The mixture was thermally treated in a tubular furnace from room temperature to 600 °C at a heating rate of 10 °C min⁻¹ and an Ar flow rate of 200 mL min⁻¹. The reaction mixture was held at this temperature (600 °C) for 2 h. The resultant product was stored in a vacuum oven at 30 °C without any washing process. In addition, GNS without sulfur was prepared by repeating the same procedure without the elemental sulfur powder.

2.2. Characterization

The topographical images of GNS and S-GNS were obtained using an atomic force microscope (NT-MDT, Russia) with a NSG-10 cantilever (NT-MDT, Russia) in semicontact operation mode. Raman measurements were performed using a NTEGRA Spectra

spectrometer (NT-MDT, Russia) equipped with a 473 nm (2.62 eV) laser in backscattering configuration. The spectral resolution was $\sim 2 \text{ cm}^{-1}$ with a 600 grooves/mm grating. A 100× objective (N.A. 0.9) provided a laser spot size of $\sim 330 \text{ nm}$. The laser power was kept well below 0.3 mW for nondestructive Raman measurements. The spectrometer was equipped with a piezoelectric scanner that allowed Raman mapping of an area up to $130 \times 130 \text{ }\mu\text{m}$. Elemental analysis (EA) was performed using an EA1112 (CE instrument, Italy). X-ray photoelectron spectroscopic analysis (XPS, PHI 5700 ESCA) was performed using monochromated Al K α radiation ($h\nu = 1486.6 \text{ eV}$). The samples for XPS measurement were pressed onto metal substrates in order to correct the charge-up. Infrared spectroscopy (IR) was performed using VERTEX 80v (Bruker Optics, Germany). To measure the electrical transport properties, S-GNS and GNS flakes were deposited on 300-nm-thick SiO_2 /highly p-doped Si wafers. The electrodes were fabricated by conventional electron beam lithography (acceleration voltage: 30 keV). Ti/Au (5/50 nm) were deposited using an e-gun evaporation system in high vacuum ($< 1 \times 10^{-3} \text{ Pa}$) and lift-off procedures. Temperature-dependent I – V characteristics were determined by the conventional two-probe method in the Janis cryogenic system with a semiconductor characterization system (4200-SCS, Keithley). The electrical measurements were performed after vacuum degassing for 12 h ($< 5 \times 10^{-4} \text{ Pa}$).

2.3. Electrochemical characterization

The electrochemical performances of GNS and S-GNS were evaluated using a Wonatec automatic battery cycler and CR2016-type coin cells. The working electrodes were prepared by mixing the active material (80 wt.%) with conductive carbon (10 wt.%) and polyvinylidene fluoride (10 wt.%) in *N*-methyl-2-pyrrolidone (NMP). The resultant slurries were uniformly applied to Cu foil. The electrodes were dried at 120 °C for 2 h and roll pressed. The coin cells were assembled in a glove box filled with argon and employing a composite electrode with metallic lithium foil and 1 M LiPF₆ (Aldrich, purity: 99.99%) dissolved in a solution of ethylene carbonate/dimethyl carbonate/diethyl carbonate (1:2:1 v/v) as the electrolyte. The cells were galvanostatically cycled between 0.01 and 3.0 V *vs.* Li/Li⁺ at various current densities.

2.4. First-principles simulation

We employed density functional theory (DFT) with Perdew–Burke–Ernzerhof (PBE) exchange correlation and all-electron-like projector-augmented plane wave (PAW) potential as implemented in the Vienna ab initio simulation package (VASP). All simulations were performed with a 6×6 graphene supercell and a vacuum region of 15 Å. A plane-wave basis set with a kinetic energy cutoff of 500 eV and a k -point grid ($4 \times 4 \times 1$) were used for total energy calculations. All structural relaxations were carried out until atomic forces became less than 0.015 eV Å⁻¹.

The thermodynamic stability of S-related defects in graphene was examined by calculating the defect formation energy,

$$E_{\text{formation}} = E_{\text{tot}} - E_{\text{graphene}} - n \times \mu_S + n \times \mu_C \quad (1)$$

where E_{tot} and E_{graphene} are the DFT total energies of the S-doped system and pristine graphene, respectively, n is the number of C atoms replaced by S, and μ_S and μ_C are the chemical potentials of S and C, respectively, taken from alpha phase bulk sulfur and pristine graphene. The S-binding energy to defect sites was also calculated using

$$E_{\text{binding}} = (E_{\text{substrate}} + E_S) - E_{\text{tot}} \quad (2)$$

where $E_{\text{substrate}}$ and E_S are the DFT total energies of defective graphene with vacancies and atomic sulfur, respectively.

3. Results and discussion

An elemental sulfur and lyophilized G–O mixture was thermally treated in a tubular furnace from room temperature to 600 °C at a heating rate of 10 °C min⁻¹ and an Ar flow rate of 200 mL min⁻¹. The reaction mixture was held at this temperature (600 °C) for 2 h. The sulfur molecules might attack the numerous defect sites in both the basal plane and the G–O edge, resulting in homogeneous doping throughout the G–O surface [15,16]. Atomic force microscopy topographic images of GNS and S-GNS show similar morphological characteristics [Fig. 1(a) and (b)]: a corrugated surface with a height of several nanometers and a lateral size of several micrometers. No significant difference is found at the Raman D-, G-,

and 2D-peak frequencies of GNS and S-GNS [Fig. 1(c)], which are, respectively, ~1368, ~1599, and ~2720 cm⁻¹. As shown in Fig. 1(c), however, the I_D/I_G ratio (D-peak intensity:G-peak intensity) in GNS (0.78) is obviously different from that in S-GNS (1.19). To clarify whether this results from spatial I_D/I_G ratio nonuniformity within the same sample, maps of the I_D/I_G ratio are examined for both GNS [Fig. 1(a)] and S-GNS [Fig. 1(b)] samples [Fig. 1(d) and (e)]. The spatial I_D/I_G ratio distributions across the GNS and S-GNS samples are relatively uniform, indicating that the difference between their I_D/I_G ratios is due to the discrepancy between the fundamental characteristics of GNS and S-GNS. Note that for both the GNS and S-GNS samples, the I_D/I_G ratio at the basal plane is comparable to that at the edge. These results suggest that sulfur doping of GNS increases defects over the entire area of the GNS [27]. Energy-dispersive X-ray spectroscopy results (Fig. S1) confirm that the sulfur is doped on the entire area of the GNS.

The sulfur-bonding configuration and elemental composition in S-GNS were investigated using XPS, IR, and EA. The XPS S 2p spectrum [Fig. 2(a)] of S-GNS shows two distinct peaks centered at 164.4 and 167.6 eV, corresponding to C–S and C–SO_x bonds [24,25], respectively. The IR spectrum of S-GNS [Fig. 2(b)] also shows the C–S stretching vibration at 877 cm⁻¹ and several new peaks at 1126, 1093, and 1048 cm⁻¹ corresponding to S=O, C=S, and sulfone bonds, respectively [28,29]. The IR spectrum of S-GNS shows notable differences when compared to that of the GNS in the range <1300 cm⁻¹, with a large C–O bond at 1223 cm⁻¹. These results are consistent with earlier reports on amorphous carbon and graphene [23–25,28–30]. But the doping content of sulfur is relatively higher when using elemental sulfur (Table 1). The sulfur content in S-GNS is found to be 4.3 at.% from XPS data and 8.7 wt.% from EA analysis, which is equivalent to C₁₉S. In addition, the sulfur content do not change in samples that were thermally treated at 800 °C [S-GNS800, Fig. 2(c)] and 1000 °C [S-GNS1000, Fig. 2(d)], although the oxygen content decreases considerably. In the XPS O 1s spectra of GNS [Fig. 2(e)], two distinct peaks (530.6 and 532.9 eV) can be observed, which are corresponding to carbonyl groups and various other oxygen groups. These two peaks are also present in the XPS spectra of S-GNS [Fig. 2(f)], but they are shifted to lower binding energy levels. This result indicates interactions between sulfur and oxygen. In addition, a significant amount of oxygen (15.1 at.%) remains in the S-GNS sample. Similar peaks are also observed in S-GNS800 and S-GNS1000. But their oxygen contents decrease considerably to 9.9 at.% (S-GNS800) and 8.9 at.% (S-GNS1000). The oxygen content in S-GNS is larger than that in GNS.

The formation mechanism of S-GNS is investigated using first-principles DFT calculations. Three prominent S defects are identified with low formation energies in graphene, i.e., (1) an S adatom on a C–C bond (S_{epi}), (2) an S adatom on a monovacancy (S_C), and (3) an S₂ dimer on a divacancy (S_{2C2}) (Fig. 3(a)) [31–33]. The S atom is buckled out of plane by 1.12 Å for S_C, and the two S atoms are oppositely buckled by 1.31 Å for S_{2C2}. The calculated formation energies are 1.59 (S_{epi}), 2.83 (S_C), and 2.64 (S_{2C2}) eV, indicating that S_{epi} is the most abundant S species. Because mono- and di-carbon vacancies may present routinely in the thermal reduction process of G–O, the formation of S_C and S_{2C2} is also very likely. In this case, the S binding energy to the defect site should be a good measure of defect stability. The calculated S binding energies are 0.85, 7.25, and 4.89 eV for S_{epi}, S_C, and S_{2C2}, respectively. Because the bulk S cohesive energy is 2.45 eV, S_{epi} is not stable against forming bulk S. In contrast, the fact that the highest binding energy of S_C surpasses the S cohesive energy implies that the substitutional S_C could be the most abundant species in S-GNS samples. The large energy gain in passivating mono- and di-vacancy defects can be attributed to the multivalent nature of S, which is different from stringent O. The additional defect stabilization by S could make the defect

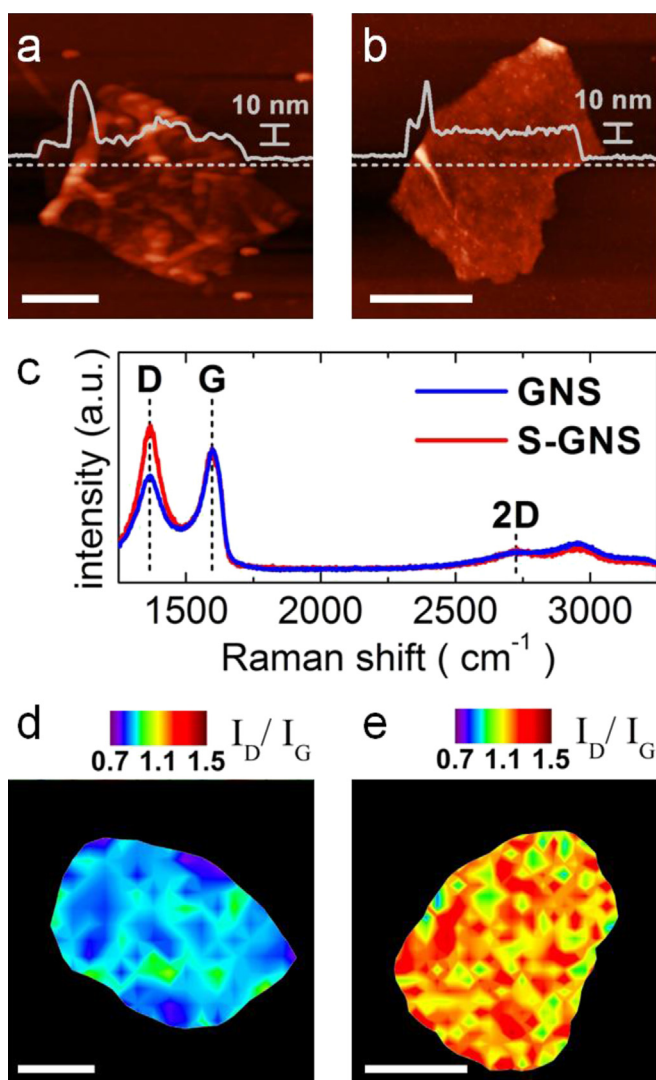


Fig. 1. Morphologies and structural characteristics of GNS and S-GNS. AFM topographic images of (a) GNS and (b) S-GNS. (c) Raman spectra of GNS (black) and S-GNS (red) measured from the samples shown in (a) and (b), respectively. Raman maps for I_D/I_G ratio for (d) GNS and (e) S-GNS. Scale bar in Figs. (a), (b), (d), and (e) indicates 1 μm. (For interpretation of the references to color in this figure legend, the reader is referred to the web version of this article.)

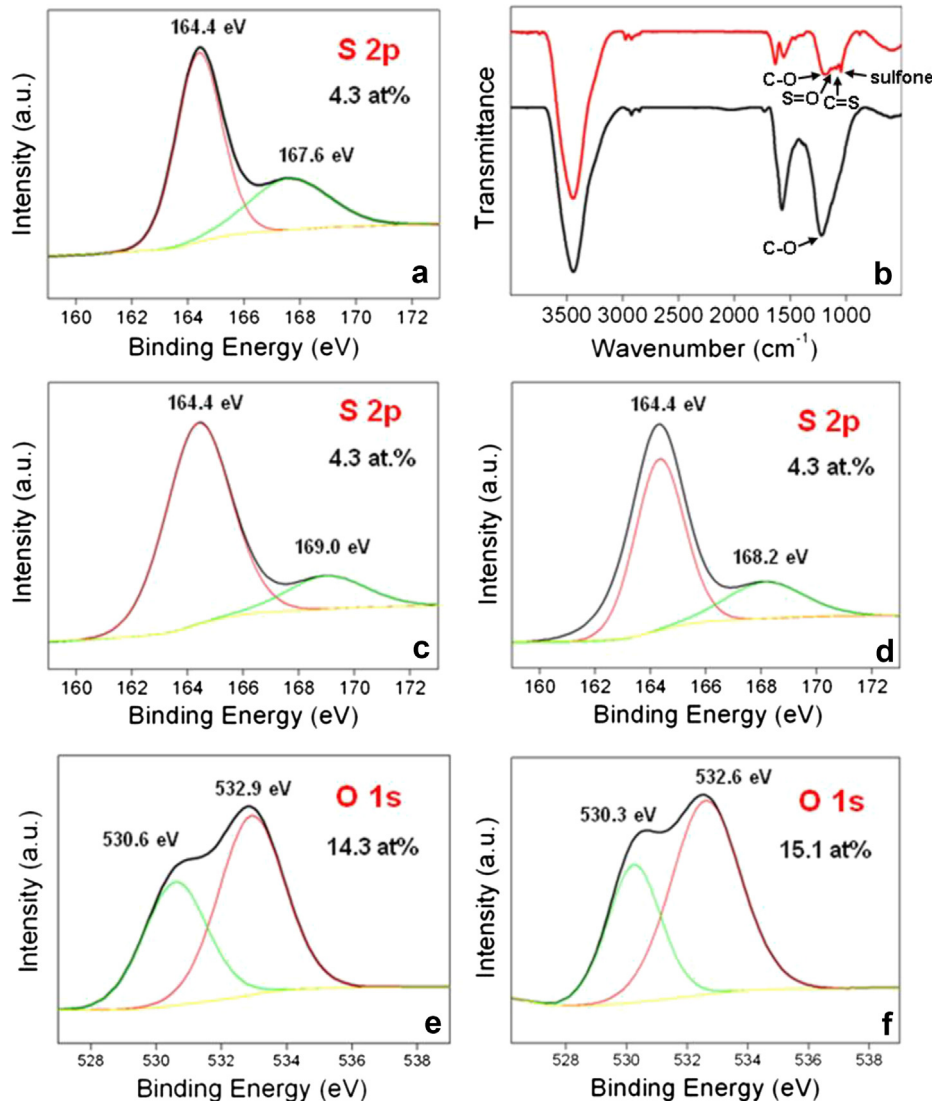


Fig. 2. Chemical bonding configurations of GNS and S-GNS. XPS S 2p spectra of (a) S-GNS, (c) S-GNS800, and (d) S-GNS1000. (b) IR spectra of GNS (black) and S-GNS (red). XPS O 1s spectra of (e) GNS and (f) S-GNS. (For interpretation of the references to color in this figure legend, the reader is referred to the web version of this article.)

concentration in S-GNS larger than that in GNS, corresponding to the reduced I_D/I_G ratio in the experiment. Because S has more electrons than C, one can expect an electron-doping effect for S replacing C as in S_C and $S2C_2$. As shown in Fig. 3(b), S_C -doped graphene is slightly electron-rich, raising the Fermi level higher than the Dirac point of pristine graphene. This is similar to the case in N-doped graphene. $S2C_2$ is almost charge-neutral, without any noticeable doping effect. This may be because the S atom in the two-fold coordination is almost self-passivated as with O [33].

The electrochemical properties of S-GNS and GNS as LIB anode materials are evaluated through constant current charge/discharge cycling in the potential range 0.01–3.0 V at various current densities. The charge/discharge curves of S-GNS and GNS [Fig. 4(a) and (c), respectively] show similar profiles with relatively large voltage hysteresis and without any distinct potential plateaus. This suggests disordered stacking of the GNS structures, resulting in electrochemically and geometrically nonequivalent Li ion sites. The voltage plateau between 0.6 and 0.7 V can be attributed to the electrolyte decomposition and solid electrolyte interface (SEI) film formation on the electrode surface [22]. Results of dQ/dV analysis for S-GNS and GNS show good agreement with the discharge/charge profiles [Fig. 4(b) and (d), respectively]. The first discharge and charge profiles of S-GNS show large specific capacities of ~ 1700 and 870 mA h g^{-1} at a current density of 374 mA g^{-1} (1 C) [Fig. 4(a) and (c), respectively]. The reversible capacity of S-GNS is more than two times that of GNS (400 mA h g^{-1}), which corresponds to $\text{Li}_{2.4}\text{C}_6$. A high reversible capacity can be induced by an increased number of active sites such as edge boundaries with chalcogens. But the more defective S-GNS800 and S-GNS-1000 samples exhibit lower reversible capacity than does S-GNS,

Table 1

Carbon, sulfur and oxygen contents from XPS and EA results.

Sample name	Atomic concentration (XPS)			Weight percent (EA)		
	C	S	O	C	S	O
GNS	85.7	–	14.3	80.1	–	17.2
GNS800	92.6	–	7.4	88.8	–	9.7
GNS1000	95.5	–	4.5	92.8	–	5.4
S-GNS	80.6	4.3	15.1	70.4	8.7	18.3
S-GNS800	85.8	4.3	9.9	76.8	8.9	12.6
S-GNS1000	86.8	4.3	8.9	78.0	9.1	11.1

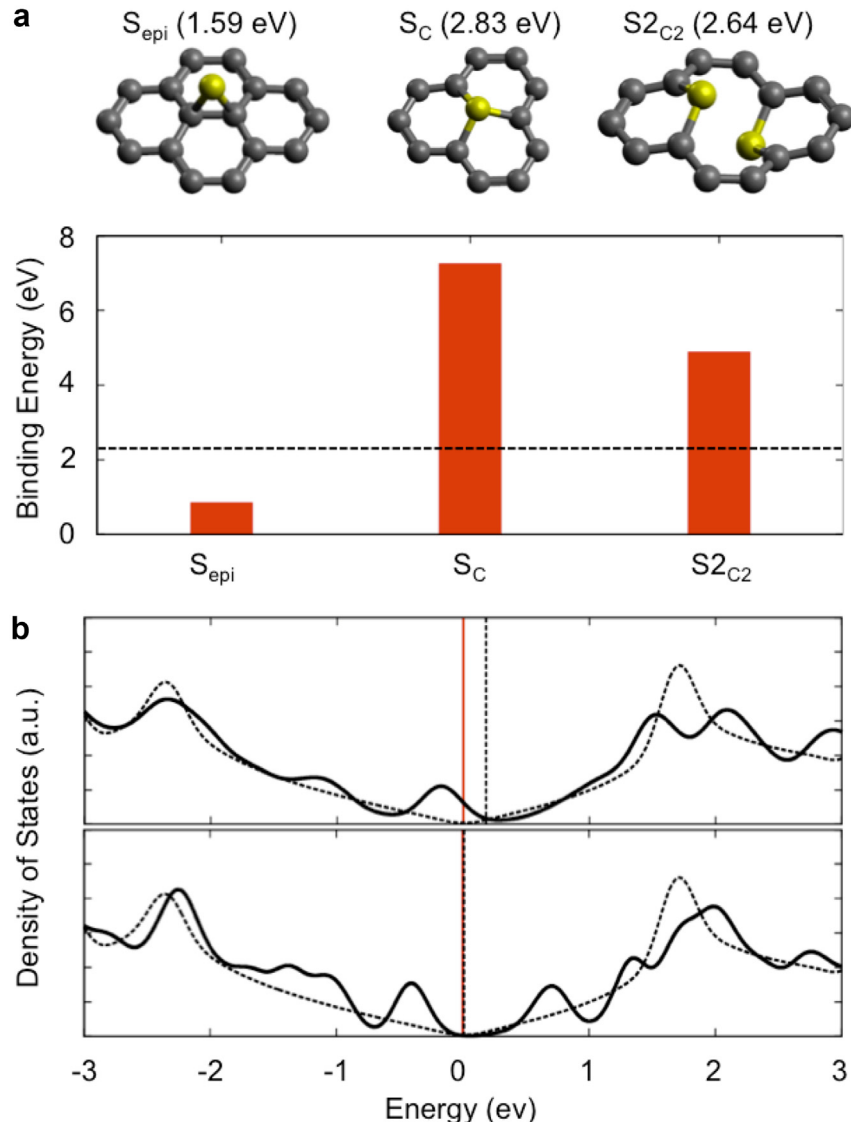


Fig. 3. First-principles calculation. (a) Atomic geometry, formation energy, and S-binding energy of S_{epi}, S_C, and S2_{C2} defects in graphene. The dashed line indicates the cohesive energy of bulk S. (b) Density of states and Fermi levels of S_C- and S2_{C2}-doped graphene as compared with those of pristine graphene. The red line indicates the location of the Dirac point. (For interpretation of the references to color in this figure legend, the reader is referred to the web version of this article.)

suggesting that heteroatoms have important effects on the reversible capacity (Fig. S2). S-GNS and GNS have similar oxygen contents, and therefore, the relatively higher reversible capacity of S-GNS results from sulfur doping. Defect sites with sulfur doping, mainly mono-C₃, contribute strongly to the reversible capacity of S-GNS via Faradaic reactions [Fig. 4(a)]. The rate performances of S-GNS and GNS from 1 to 30C are shown in Fig. 4(e). Highly stable capacities of c.a. 285 mA h g⁻¹ can still be obtained at a rate of 30 C, which is approximately three times higher than the value for GNS anode materials. In addition, when the current density returns to 8 and 10 C after 40 cycles, S-GNS successfully recovers its initial capacity, demonstrating very good reversibility. GNS also exhibits good rate capability and reversibility. But the overall capacity of GNS is found to be less than half that of S-GNS. These results indicate that S-GNS shows kinetically fast Li ions and electron conduction. In addition, with an increase in C-rate, the capacity gap between S-GNS and GNS increases further. At 30 C, the capacity of S-GNS is approximately three times higher than that of GNS (89 mA h g⁻¹). This superior rate performance of S-

GNS is attributable to its relatively better electrical properties, as supported by the following.

The temperature-dependent electrical transport properties of S-GNS and GNS are shown in Fig. 5(a) and (b), respectively. For both samples, the I–V characteristics show highly symmetric and linear behavior throughout the different temperature regions. The conductivity [$\sigma(T)$] decreases with a decrease in temperature [Fig. 5(c)], indicating nonmetallic behavior. Interestingly, although the I_D/I_G ratio in the Raman spectra increases with sulfur doping, $\sigma(T)$ of S-GNS is larger than that of GNS. At room temperature, the conductivity of S-GNS and GNS was found to be 1743 and 32 S m⁻¹, respectively. It is noteworthy that ideal two-dimensional graphene with no wrinkles, ripples, or distortion has very high mobility [34–37]. High mobility is related to high conductivity as defined by the relation $\sigma = ne\mu$. An examination of the electronic structure of S-GNS [Fig. 3(b)] shows that S_C-doped graphene is slightly electron doped. With six valence electrons, S has sufficient electrons to passivate the mono-vacancy pore, which requires four electrons ($=3 \times 4/3$). The remaining electrons of S then become free carriers,

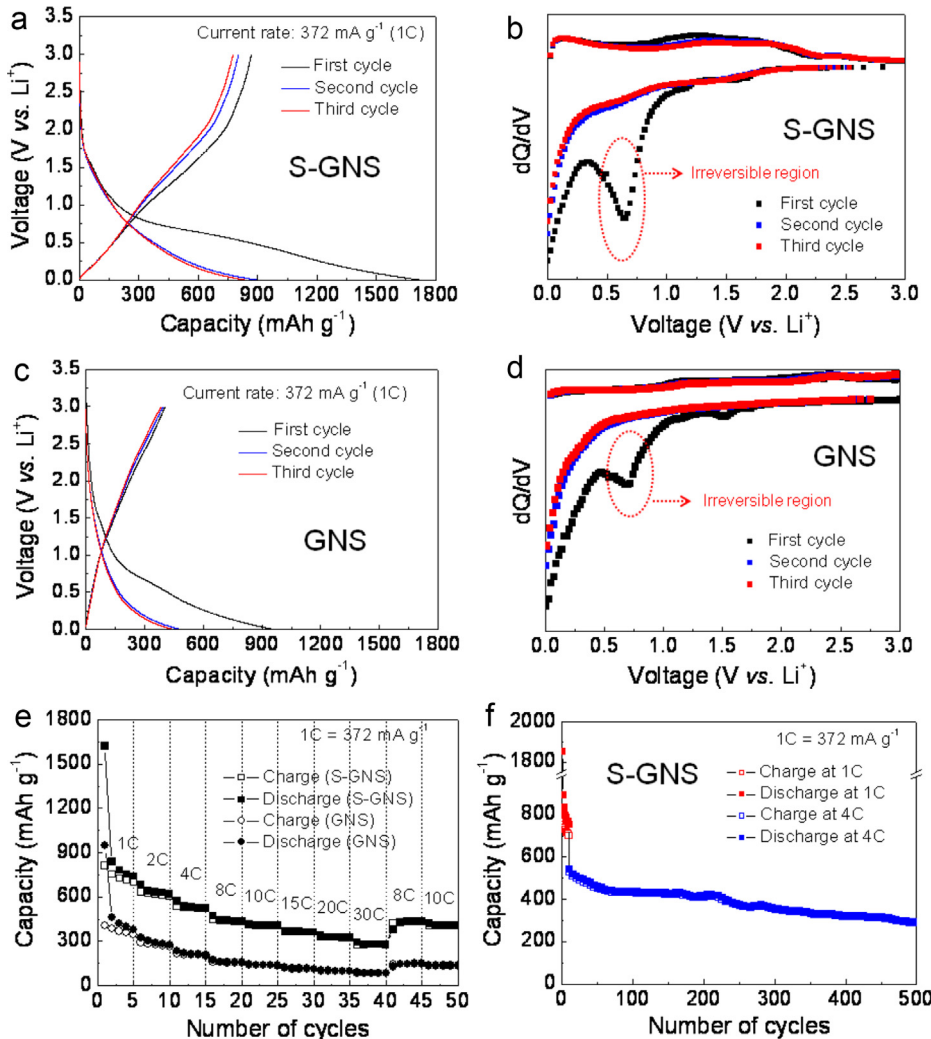


Fig. 4. Electrochemical performance of S-GNS and GNS. Galvanostatic charge/discharge profiles of (a) S-GNS and (c) GNS in the potential range from 0.01 to 3.0 V vs. Li/Li⁺ at a current density of 372 mA g⁻¹ (1C). Results of dQ/dV analysis for (b) S-GNS and (d) GNS. (e) Rate capability of S-GNS and GNS at a various current densities from 372 mA g⁻¹ (1C) to 11160 mA g⁻¹ (30C). (f) Cycling performance of S-GNS for 500 cycles at a current density of 1488 mA g⁻¹ (4C) and after 10 cycles at a current density of 372 mA g⁻¹ (1C).

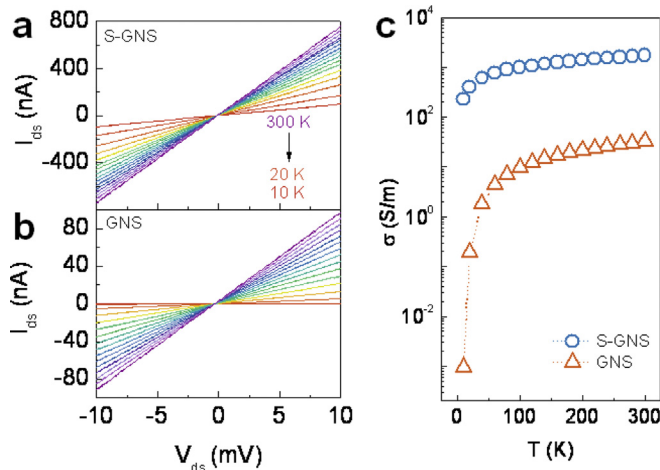


Fig. 5. Temperature-dependent electrical transport properties of S-GNS and GNS. $I-V$ characteristics of (a) S-GNS and (b) GNS measured from 300 K to 10 K with a step of 20 K (exception: 20 K–10 K). (c) Temperature-dependent conductivity curves obtained from $I-V$ curves. Circles and triangles denote S-GNS and GNS, respectively.

contributing to the overall conductivity of S-GNS. In this light, it is also possible that the flat surface of S-GNS is the key factor responsible for the high conductivity. This behavior is clearly observed in the line profiles obtained from the AFM study, as shown in Fig. 1(a) and (b). On this basis, we postulate that the high electrochemical performance of S-GNS originates from its high conductivity. The cycling stability of S-GNS is tested for 500 cycles at a current density of 1488 mA g⁻¹ (4C) after 10 cycles at a current density of 372 mA g⁻¹ (1C) [Fig. 4(f)]. The cyclic stability is maintained during the 500 cycles. Despite the high rate of 4C, a specific capacity of ~ 290 mA h g⁻¹ is achieved after 500 cycles.

4. Summary

Sulfur-doped graphene-based nanosheets are successfully prepared by the thermal treatment of elemental sulfur and lyophilized G–O mixtures. Sulfur is uniformly deposited over the entire area of GNS as defects. In addition, numerous oxygen heteroatoms remain in the S-GNS sample despite thermal treatment with elemental sulfur. DFT calculations show that substitutional Sc replacing a single C atom in graphene can be the most abundant defects in this experiment. The electronic structure of Sc-doped graphene is

slightly electron doped, contributing to the overall conductivity as well as the flat S-GNS surface. The electrochemical performance of S-GNS is superior to that of GNS. The reversible capacity of S-GNS is two and three times that of GNS at current densities of 372 mA g⁻¹ (1 C) and 11,160 mA g⁻¹ (30 C), respectively. The high capacitance of S-GNS can result from increased lithium-insertion active sites such as edge boundaries on doping with chalcogens. The excellent rate performance of S-GNS can be attributed to its good electrical properties. Cyclic stability is maintained even for up to 500 charge/discharge cycles at a high rate of 4 C, despite the presence of numerous chalcogen heteroatoms and defects.

Acknowledgments

This work was supported by the National Research Foundation of Korea Grant funded by the Korean government (MEST) (NRF-2010-C1AAA001-0029018). Work at KAIST was supported by the Institute for Basic Science (IBS) (CA-1201-02) and Global Frontier R&D (2011-0031566: Center for Multiscale Energy Systems) programs funded by the Korea government (MEST).

Appendix A. Supplementary data

Supplementary data related to this article can be found at <http://dx.doi.org/10.1016/j.jpowsour.2014.03.084>.

References

- [1] J. Tollefson, *Nature* 456 (2008) 436–440.
- [2] J.M. Tarascon, M. Armand, *Nature* 414 (2001) 359–367.
- [3] K. Kang, Y.S. Meng, J. Breger, C.P. Grey, G. Ceder, *Science* 311 (2006) 977–980.
- [4] M. Armand, J.M. Tarascon, *Nature* 451 (2008) 652–657.
- [5] K. Sawai, T. Ohzuku, *J. Electrochem. Soc.* 150 (2003) A674–A678.
- [6] B. Guo, X. Wang, P.F. Fulvio, M. Chi, S.M. Mahurin, X.G. Sun, S. Dai, *Adv. Mater.* 23 (2011) 4661–4666.
- [7] A.K. Geim, K.S. Novoselov, *Nat. Mater.* 6 (2007) 183–191.
- [8] A.K. Geim, *Science* 324 (2009) 1530–1534.
- [9] Y. Zhu, S. Murali, W. Cai, X. Li, J.W. Suk, J.R. Potts, R.S. Ruoff, *Adv. Mater.* 22 (2010) 3906–3924.
- [10] J.R. Dahn, T. Zheng, Y. Liu, J.S. Xue, *Science* 270 (1995) 590–593.
- [11] Y. Liu, J.S. Xue, T. Zheng, J.R. Dahn, *Carbon* 34 (1996) 193–200.
- [12] M. Liang, L. Zhi, *J. Mater. Chem.* 19 (2009) 5871–5878.
- [13] N.A. Kaskhedikar, J. Maier, *Adv. Mater.* 21 (2009) 2664–2680.
- [14] M. Winter, J.O. Besenhard, M.E. Spahr, P. Novák, *Adv. Mater.* 10 (1998) 725–763.
- [15] K. Erickson, R. Erni, Z. Lee, N. Alem, W. Gannett, A. Zettl, *Adv. Mater.* 22 (2010) 4467–4472.
- [16] C. Gómez-Navarro, J.C. Meyer, R.S. Sundaram, A. Chuvilin, S. Kurasch, M. Burghard, K. Kern, U. Kaiser, *Nano Lett.* 10 (2010) 1144–1148.
- [17] C. Uthaisar, V. Barone, *Nano Lett.* 10 (2010) 2838–2842.
- [18] Y.G. Guo, J.S. Hu, L.J. Wan, *Adv. Mater.* 20 (2008) 2878–2887.
- [19] G. Wang, X. Shen, J. Yao, J. Park, *Carbon* 47 (2009) 2049–2053.
- [20] E. Yoo, J. Kim, E. Hosono, H.S. Zhou, T. Kudo, I. Honma, *Nano Lett.* 8 (2008) 2277–2282.
- [21] D. Pan, S. Wang, B. Zhao, M. Wu, H. Zhang, Y. Wang, Z. Jiao, *Chem. Mater.* 21 (2009) 3136–3142.
- [22] P. Guo, H. Song, X. Chen, *Electrochem. Commun.* 11 (2009) 1320–1324.
- [23] S. Ito, T. Murata, M. Hasegawa, Y. Bito, Y. Toyoguchi, *J. Power Sources* 68 (1997) 245–248.
- [24] Y.P. Wu, S. Fang, Y. Jiang, R. Holze, *J. Power Sources* 108 (2002) 245–249.
- [25] Y. Yan, Y.X. Yin, S. Xin, Y.G. Guo, L.J. Wan, *Chem. Commun.* 48 (2012) 10663–10665.
- [26] Y.S. Yun, Y.H. Bae, D.H. Kim, J.Y. Lee, I.J. Chin, H.J. Jin, *Carbon* 49 (2011) 3553–3559.
- [27] L. Zhao, R. He, K.T. Rim, T. Schiros, K.S. Kim, H. Zhou, C. Gutiérrez, S.P. Chockalingam, C.J. Arguello, L. Pálová, D. Nordlund, M.S. Hybertsen, D.R. Reichman, T.F. Heinz, P. Kim, A. Pinczuk, G.W. Flynn, A.N. Pasupathy, *Science* 333 (2011) 999–1003.
- [28] A. Macías-García, C. Valenzuela-Calahorro, V. Gómez-Serrano, *Carbon* 31 (1993) 1249–1255.
- [29] J. Zawadzki, *Carbon* 25 (1987) 431–436.
- [30] Z. Yang, Z. Yao, G. Li, G. Fang, H. Nie, Z. Liu, X. Zhou, X. Chen, S. Huang, *ACS Nano* 6 (2012) 205–211.
- [31] W.I. Choi, S.H. Jhi, K. Kim, Y.H. Kim, *Phys. Rev. B* 81 (2010) 085441.
- [32] D.H. Lee, W.J. Lee, S.O. Kim, Y.H. Kim, *Phys. Rev. Lett.* 106 (2011) 175502.
- [33] A.T. Lee, J. Kang, S.H. Wei, K.J. Chang, Y.H. Kim, *Phys. Rev. B* 86 (2012) 165403.
- [34] J. Xue, J. Sanchez-Yamagishi, D. Bulmash, P. Jacquiod, A. Deshpande, K. Watanabe, T. Taniguchi, P. Jarillo-Herrero, B.J. LeRoy, *Nat. Mater.* 10 (2011) 282–285.
- [35] W. Gannett, W. Regan, K. Watanabe, T. Taniguchi, M.F. Crommie, A. Zettl, *Appl. Phys. Lett.* 98 (2011) 242105.
- [36] C.R. Dean, A.F. Young, I. Meric, C. Lee, L. Wang, S. Sorgenfrei, K. Watanabe, T. Taniguchi, P. Kim, K.L. Shepard, J. Hone, *Nat. Nanotechnol.* 5 (2010) 722–726.
- [37] J. Sławińska, I. Zasada, P. Kosinski, Z. Klusek, *Phys. Rev. B* 82 (2010) 085431.